A dual-phase electrolyte for high-energy lithium-sulfur batteries

*Yuxun Ren, Arumugam Manthiram**

Materials Science & Engineering Program and Texas Materials Institute
The University of Texas at Austin, Austin, TX, 78721, USA
*Corresponding author: Tel: +1-512-471-1791; fax: +1-512-471-7681
E-mail: manth@austin.utexas.edu (A. Manthiram)

Key words: lithium-metal batteries, liquid electrolyte, pouch cell, phase separation, electrochemistry

Abstract

Dissolution of lithium polysulfides is essential for fast cathode kinetics, but detrimental for anode stability, especially under lean electrolyte conditions. In this work, we utilize the phase separation phenomenon between solvents with different polarities (tetramethyl sulfone and dibutyl ether) to enable the design of a dual-phase electrolyte. High-polarity, high-density tetramethyl sulfone - lithium bis(trifluoromethanesulfonyl)imide - ammonium trifluoroacetate as the cathode electrolyte strongly solvates lithium polysulfides, which propels the sulfur redox reaction. Moreover, the composite of dibutyl ether and a polymeric ion conductor serves as the anode electrolyte. The addition of dibutyl ether in the anode side effectively prevents the crossover of corrosive species (lithium polysulfides and ammonia trifluoroacetate), enabling a significant improvement in Li-metal anode stability. The electrode-specific dual-phase electrolyte design provides electrochemical performance superior to conventional electrolytes. Without additional electrode engineering, pouch cells assembled with the dual-phase electrolyte cycle under a lean electrolyte (4.0 µL mg^{-1}) and low-Li-excess condition (N/P = 3) for 120 cycles.

1. Introduction

The lithiation of sulfur in the liquid electrolyte system undergoes a solid-liquid-solid reaction pathway, with the formation of Li_2S as the final product and lithium polysulfides as intermediates.[1–3] While being an enabler for fast sulfur conversion kinetics, the dissolution of lithium polysulfide (LiPS) intermediates into the liquid electrolyte is detrimental to the stability of Li-metal anode.[4] When the electrolyte to sulfur (E/S) ratio is maintained at a practical level (e.g., 5 μL mg^{-1}) to reach a reasonable energy density, most cells suffer from fast decay within 100 cycles. This is because in the conventional liquid electrolyte system with a low E/S ratio, (i) the electrolyte containing a high concentration of lithium polysulfides is highly corrosive for Li-metal anode,[5,6] and (ii) the kinetics of sulfur redox reaction is sluggish under lean electrolyte conditions, leading to significant non-uniformity in the cell. Due to the excessive addition of liquid electrolyte, there is a huge gap currently between the practical and theoretical volumetric energy densities of Li-S system.[7–9]

The target of electrolyte engineering is to make Li-metal anode compatible with lean electrolyte conditions while ensuring fast cathode kinetics. One intensively explored direction of electrolyte design is to prevent lithium polysulfide dissolution, which extends the cycle lifetime of Li-metal anode. This goal can be attained by employing encapsulated sulfur cathodes and sparingly solvating electrolytes.[10,11] Unfortunately, such an approach sacrifices the kinetics of sulfur redox reactions and usually requires a relatively high operating temperature (e.g., 60 °C) to propel the cathode reactions. In another direction, the solvation structure of dissolved lithium polysulfides is being tailored to meet the requirements of anode stability.[12,13] For example, the substitution of chalcogen elements (e.g., tellurium) into polysulfide molecules results in a significant improvement

in anode stability.[14] However, at this stage, rather few existing electrolyte-tailoring strategies meet the requirements of anode stability and cathode kinetics synergistically.

Considering the conflicts in electrolyte requirement for anode and cathode, decoupling the anode and cathode electrolytes provides a third pathway toward high-performance lithium-sulfur batteries. The use of a dual-phase solid (inorganic or polymer) || liquid electrolyte system potentially mitigates lithium polysulfide crossover and enables fast cathode kinetics. However, with the inorganic solid electrolyte at the anode side, the anode interfacial stability becomes a concern. The solid polymer electrolyte at the anode side suffers from swelling and lithium polysulfide crossover during long-term cycling.[16] Beyond these two, a less-explored option is a thermodynamically immiscible liquid || liquid electrolyte system. Although the concept of dual-phase liquid-based electrolyte has been reported,[17,18] there is no successful demonstration with Li-S batteries. Cho et al. reported the combination of 1.0 LiTFSI in ethyl methyl sulfone (EMS) and 2.3 M LiTFSI in tetraglyme to form a thermally immiscible dual-phase electrolyte for Li-S batteries.[19] The central issue of this design is that (i) tetraglyme as the anode electrolyte does not fully prevent the dissolution of lithium polysulfides and (ii) with the solvation of lithium polysulfides, the density of EMS-based cathode electrolyte increases and eventually becomes the high-density phase that will mix with the tetraglyme anode electrolyte.

Motivated by these challenges, we propose a new dual-phase electrolyte design strategy, which is enabled by the complete phase separation between low-density dibutyl ether (DBE) and high-density tetramethyl sulfone (TMS). There are two ion-conducting immiscible liquid-based electrolyte layers in the cell. The top phase is a composite of solid polymer ion conductor and DBE-LiTFSI, and the bottom phase is the TMS-LiTFSI. The two electrolyte layers are seamlessly connected in series, showing a low interfacial resistance (1.7 Ohm cm^2). This approach results in

immiscible electrolyte layers with no concerns of electrolyte interdiffusion and lithium polysulfide crossover. Moreover, the highly solvating TMS-based cathode electrolyte enables a facile dissolution of lithium polysulfides. By decoupling the solvents of anode and cathode electrolytes, the low-Li-excess (N/P = 3) and lean electrolyte (4.0 μL mg^{-1}) pouch cell can maintain above 72% of its initial capacity after 120 cycles.

2. Result and discussion

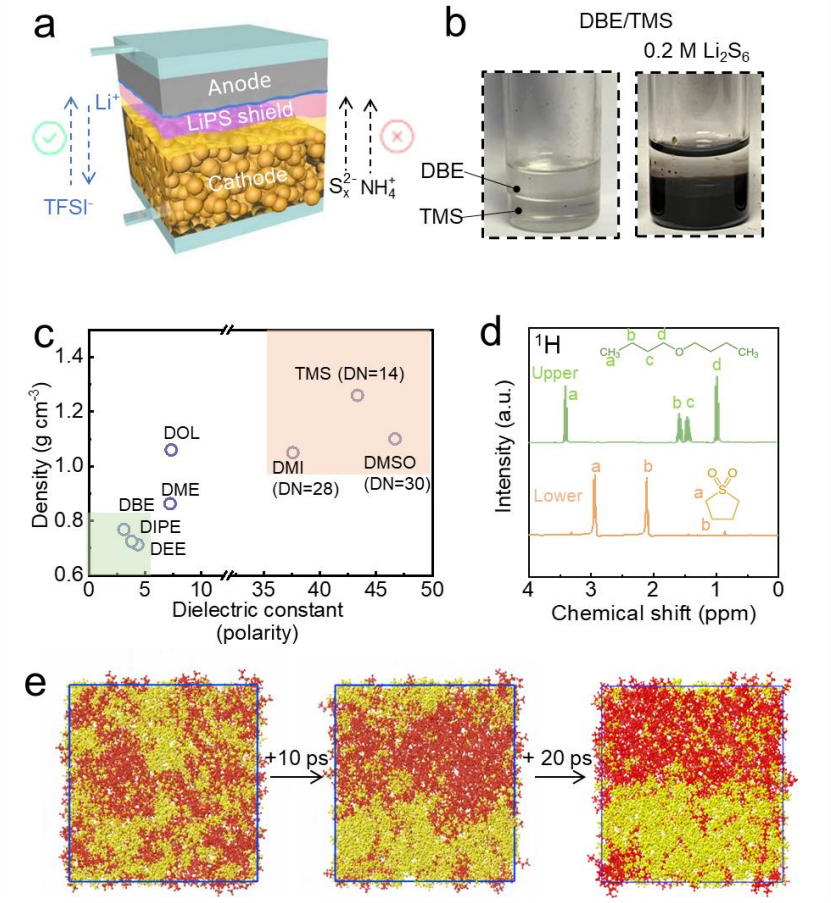

Figure 1. Design of the dual-phase electrolyte. (a) Schematic of the lithium-sulfur cell with dual-phase liquid electrolyte. (b) Photos showing the immiscibility of Li_2S_6 in TMS solution and DBE. (c) Diagram showing the density and dielectric constant of various solvents. (d) ^1H NMR spectra of upper and lower phases of solvents (according to photo in Figure 1b). (e) Molecular dynamic simulation result showing the extremely fast phase separation of DBE and TMS in 20 ps (1 ps = 10^{-12} s). DBE molecules display red color, while TMS molecules display yellow color.

The cell configuration is shown in **Figure 1**a. A gel polymer electrolyte that can prevent corrosive species crossover was attached to the Li-metal anode while a strongly solvating liquid electrolyte was added into the sulfur cathode. To prevent the LiPS crossover, we screened the polarity of various solvents and identified dibutyl ether and tetramethyl sulfone as a solvent couple that is entirely immiscible (Figure 1b). In addition to the difference in polarity, DBE and TMS display different mass densities. The strongly solvating TMS is heavier (1.26 g cm^{-3}) while the weakly solvating DBE is lighter (0.77 g cm^{-3}). This benefits the phase separation in the electrochemical cell. Addition of lithium salt does not alter the phase separation behavior (Figure S1, Supporting Information). Diisopropyl ether (DIPE) and diethyl ether (DEE) with polarity and density close to DBE also display phase separation with TMS, while 1,2-dimethoxyethane (DME) and 1,3-dioxolane (DOL) with a moderate polarity are both mixed with TMS (Figure S1, Supporting Information).

The ^{1}H nuclear magnetic resonance (NMR) spectra in Figure 1d display the characteristic peaks of DBE for the top phase, whereas those peaks of TMS appear only for the bottom phase. Molecular dynamics (MD) simulations were conducted to quantify the interfacial tension between these two liquid phases. Consistent with the experimental observations, the pre-mixed two phases separated extremely fast according to the simulation (20 ps). The interfacial tension as a descriptor reached 0.86 mN m^{-1}, exceeding the reported value for EMS/TEGDME (0.58 mN m^{-1}) electrolyte system (Figure S2, Supporting Information).[19] The immiscibility of these two phases minimized the contact surface area between anode and cathode electrolytes.

In a real electrochemical cell, liquid DBE-LiTFSI is combined with an *in-situ* derived polymer ion conductor and a polymer matrix to derive a gel polymer electrolyte (GPE). This process is required because, first, during the cell assembly process, the porous structure of separator

and electrode can induce a capillary flow of liquids.[20,21] Once DBE-LiTFSI is confined in the polymer matrix, it is unlikely going to migrate into the cathode. Second, in the DBE/TMS system, due to the difference in solvating power, DBE cannot not solvate enough Li salt to ensure fast ion transport.

To immobilize the liquid DBE-LiTFSI, the gel polymer electrolyte was derived from the thermally-induced polymerization of the liquid precursor (see details in Experimental method). The GPE is composed of three compositions: poly(1,3-dioxolane)-LiTFSI and DBE-LiTFSI as the ion conductors and poly (pentaerythritol tetraacrylate) as the polymer matrix. The *in-situ* derived poly (PETEA) matrix prevents the phase separation of poly(1,3-dioxolane)-LiTFSI and liquid DBE-LiTFSI during the thermal-curing process.[22] Although DBE-LiTFSI is still in its liquid phase, the binding between DBE molecules and polymer matrix (polyDOL and PETEA) in GPE effectively prevents DBE from migrating into the cathode.

We further considered the capability of GPE to transport Li^+ ion and prevent lithium polysulfide crossover. Considering the difference in the solvating power, the Li salt is inclined to distribute non-uniformly across the two phases. Although DBE solvates LiTFSI (up to 3.0 M solubility), the Li salt concentration in DBE phase decreases to a non-detectable level (according to ^{19}F NMR spectra) when an equivalent volume of TMS is added, which is because of the significant difference of solvating power between TMS and DBE. The polymer ion conductor (polyDOL-LiTFSI) in GPE is essential for retaining the Li salt since polyDOL has a moderate polarity (dielectric constant) and reasonable solvating power (**Figure 2**a).[23] After putting the same volume of GPE and TMS-LiTFSI with the same lithium salt concentration (1.0 M) together for over one week, ^{19}F NMR shows the GPE still contains 0.83 M of LiTFSI, which ensures reasonably fast Li^+ ion transport.

To further understand the interfacial resistance, we reveal that for one layer of Celgard 2500 immersed with GPE (poly(DOL)/DBE-LiTFSI) or TMS-LiTFSI (both with 1.0 M LiTFSI), the areal resistance is 19.6 Ohm cm^2 and 4.9 Ohm cm^2, respectively (Figure 2b). When stacking these two layers together, the overall resistance becomes 27.2 Ohm cm^2. The interfacial resistance between GPE and liquid TMS-LiTFSI can be derived as 2.7 Ohm cm^2 (Figure 2b).

Like almost all polymer ion conductors, polyDOL displays a high affinity with the highly polar TMS, leading to significant swelling of GPE. Moreover, polyDOL solvates lithium polysulfides very easily (Figure 2c d). For the GPE filled with DBE-LiTFSI, the lithium polysulfide crossover problem is resolved because DBE repels TMS out of the GPE (see Figure 2d and Figure S1c), even when the GPE is in the bottom of the vial.

Sulfur cathode requires high ion mobility and low viscosity for faster kinetics.[24,25] Due to strong electrostatic interactions between the positively charged Li^+ and negatively charged terminal sulfur of polysulfide molecules, a cluster consisting of multiple lithium polysulfide molecules is found to be a more stable configuration than discrete, isolated polysulfide chains. The formation of the lithium polysulfide cluster results in a lower solubility and inferior cathode kinetics. Therefore, one direction to boost kinetics is to employ additives that can weaken the Li^+-S^- binding and promotes lithium polysulfide dissolution.

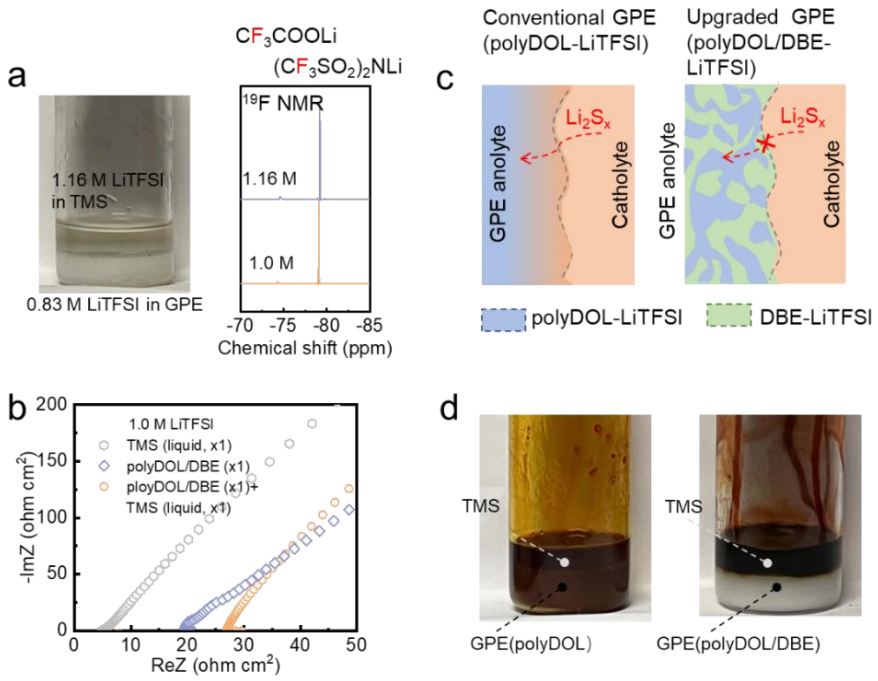

Figure 2. Interfacial resistance within the dual-phase electrolytes. (a) ^{19}F NMR measurement of the Li salt concentration in the TMS-LiTFSI phase. (b) EIS profiles, showing the areal resistances of electrolyte-immersed separator. (c) Schematic showing the difference between conventional GPE and upgraded GPE (with DBE) in reducing lithium polysulfide crossover. (d) Diffusion experiments (12 hours) showing the swelling behavior of GPE without DBE, and phase separation of GPE (with DBE) and TMS. 0.2 M Li_2S_6 was dissolved in TMS. The

Inspired by the previous work in the literature, we reveal that ammonium trifluoroacetate (CF_3COONH_4, NH_4TFA) is a feasible low-cost additive for propelling sulfur redox reaction.[26–28] NH_4TFA dissociates to NH_4^+ cation and TFA^- anion in liquid electrolyte, which spontaneously reacts with lithium polysulfides to form diammonium polysulfides and LiTFA. This reaction prevents the clustering induced by the coordination between Li^+ and terminal sulfur. However, NH_4TFA additive is detrimental to the cyclability of Li-metal anode, since NH_4^+ cation can be reduced by Li-metal to form insulating LiH or $LiNH_2$ species.[29] Ideally, NH_4TFA additive needs to be confined within the cathode region to prevent anode corrosion.

As shown in **Figure 3**a, the addition of NH_4TFA in TMS (> 0.2 M solubility) changes the color of lithium polysulfide solution from dark grey to orange-red. Further addition of DBE does not alter the solution color, which is due to the insolubility of NH_4TFA in DBE. This was further confirmed by ^1H NMR spectra, where no peak can be assigned to NH_4^+ cation (Figure S3, Supporting Information). Because of the large size of NH_4^+ cation (147 pm versus 76 pm for Li^+), DBE solvent molecules cannot overcome the lattice energy to dissociate the NH_4TFA salt.

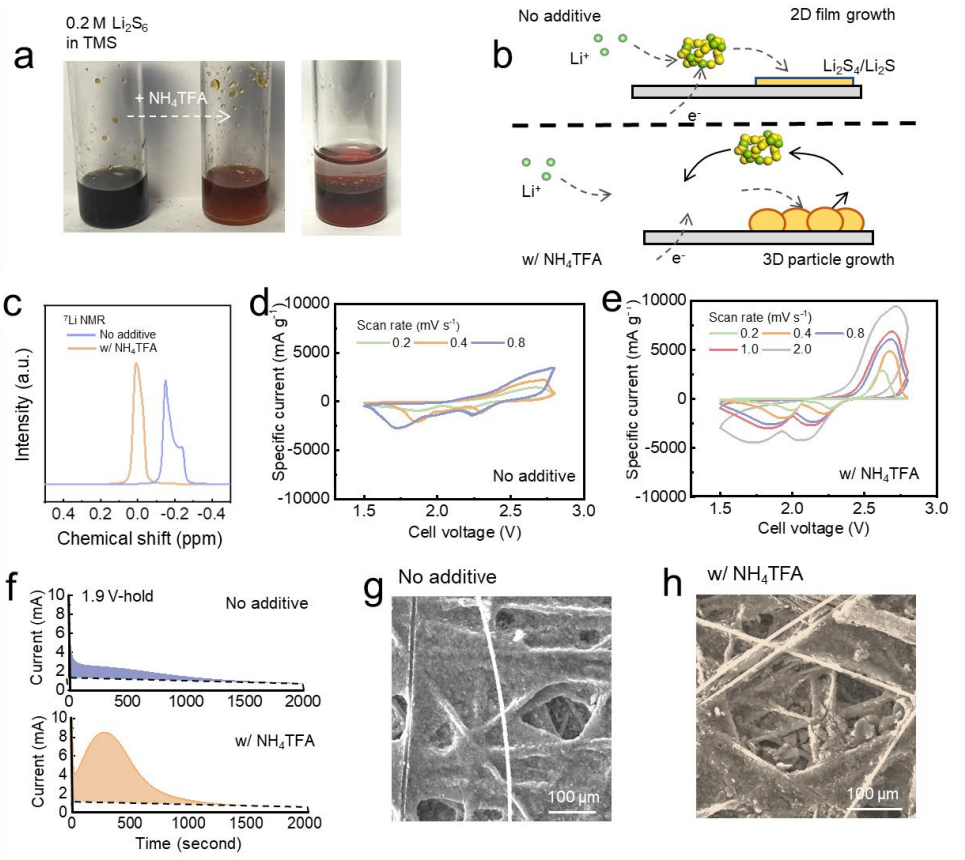

Figure 3. Kinetics of sulfur cathode. (a) Photos showing the Li_2S_6 solution color change induced by NH_4TFA. There was no further color change after the addition of DBE. (b) Schematics showing the difference of Li_2S deposition with and without NH_4TFA additive. (c) ^7Li NMR of 0.2 M Li_2S_6 in TMS with and without 0.4 M NH_4TFA. (d, e) Cyclic voltammetry profiles of Li-S cells based on the dual-phase electrolyte with and without NH_4TFA additive. (f) Chronoamperometry experiments. The cell was discharged to 2.1 V and held at 1.9 V until the current decreased to 10^{-3} mA. (g, h) SEM images of the discharged electrodes from Li-S cells with and without NH_4TFA.

Under the lean electrolyte condition, various analytical techniques further validate the enhancement of sulfur utilization induced by NH_4TFA. The ^7Li NMR characterization further validates that the addition of NH_4TFA suppresses the clustering of lithium polysulfides and benefits the transport of Li^+ from the liquid electrolyte solution into the lithium polysulfide chains (Figure 3c). With lithium polysulfide clustering prevented by the addition of NH_4TFA, the peak was heightened. Moreover, the peak shifted downfield (towards a more positive position), since the Li^+ nuclei in solution is deshielded, in consistent with what literature observed previously.[26]

As shown in **Figure 3**a, the addition of NH_4TFA in TMS (> 0.2 M solubility) changes the color of lithium polysulfide solution from dark grey to orange red. Addition of DBE does not alter the solution color, which is due to the insolubility of NH_4TFA in DBE. This was further confirmed by ^1H NMR spectra, where no peak can be assigned to NH_4^+ cation (Figure S3). Because of the large size of NH_4^+ cation (147 pm versus 76 pm for Li^+), DBE solvent molecules cannot overcome the lattice energy to dissociate the NH_4TFA salt.

Under the lean electrolyte condition, various analytical techniques validate the enhancement of sulfur utilization induced by NH_4TFA. The ^7Li NMR characterization further validates that the addition of NH_4TFA suppresses the clustering of lithium polysulfides and benefits the transport of Li^+ from the liquid electrolyte solution into the lithium polysulfide chains (Figure 3c). With lithium polysulfide clustering prevented by the addition of NH_4TFA, the peak was heightened. Moreover, the peak shifted downfield (towards a more positive position), since the Li^+ nuclei in solution is deshielded, in consistent with what literature observed previously.[26]

The higher Li^+ mobility indued by additive benefits the kinetics of sulfur conversion. According to the nucleation and growth model of Li_2S deposition, the fast kinetics leads to smaller surface overpotential and thus lower nucleation rate of Li_2S, promoting the growth of Li_2S particles

(see summary schematic in Figure 3b). In contrast, sluggish cathode kinetics results in Li_2S film deposition, leading to electrode surface passivation at a low capacity (Figure 3b) Cyclic voltammetry profile obtained at different scan rates serve as a direct confirmation of the enhancement in charge transfer and redox kinetics under the presence of NH_4TFA additive (Figure 3d, e). Chronoamperometry experiments were conducted on Li–S cells and the morphology of discharge product was compared (Figure 3f-h). NH_4TFA additive enables a much higher peak current compared with that without additive. Moreover, within the void of the carbon paper, the precipitates grew into large-sized particles (Figure 3g, h).

The kinetics of sulfur redox reactions was further investigated with *operando* XRD (**Figure 4**). [30] Precipitation of lithium polysulfides out of the liquid electrolyte was a non-negligible issue affecting the sulfur utilization under lean electrolyte condition. *Operando* XRD clearly shows the difference in sulfur utilization since it is a highly sensitive tool for LiPS detection. The peak located at 26.5° is attributed to LiPS cluster.[30] Conversion from sulfur to LiPS was clearly captured by the *operando* XRD, suggesting the resolution of the measurement is high enough. With standard electrolyte, there was a significant amount of LiPS residue after complete discharge (Figure 4a-c). In contrast, the cell with NH_4TFA shows a much-enhanced conversion from LiPS to Li_2S. The peak from LiPS vanished when the cell was fully discharged to 1.7 V (Figure 4d-f). Interestingly, there was relatively weak XRD signal for Li_2S at 27.0° for both samples, which is correlated with the previous finding that the high-polarity electrolyte facilitates the formation of amorphous discharge product.[31,32]

The stability of the Li-metal anode against liquid electrolytes is crucial for long-term cycling of pouch cells. The Li || Ni half-cell was fabricated to compare the coulombic efficiency of Li stripping/plating with different electrolytes, including DBE-LiTFSI, GPE (poly(DOL)/DBE-LiTFSI), TMS-LiTFSI, and TMS-LiTFSI/NH_4TFA. The DBE-LiTFSI or TMS-LiTFSI electrolyte

result in an average (from 20 to 100th cycle) coulombic efficiency of 90.7% and 62.2%, respectively (Figure S4, Supporting Information). The GPE-protected Ni foil achieves the highest average coulombic efficiency of 98.8% (from 20 to 100th cycle) cycles. Moreover, a significant morphology difference was observed for the Li deposit derived from GPE and TMS. GPE results in a highly conformal and uniform surface morphology, while the Li deposit derived from TMS displays dendritic features, even at a rather small capacity (0.5 mAh cm^{-2}). Clearly, ether performs better to stabilize the Li metal anode, since ether is more stable against reduction and facilitates the formation of inorganic SEI.[33] The polymer matrix in GPE also improves the mechanical stability of SEI, contributing to the improved coulombic efficiency.

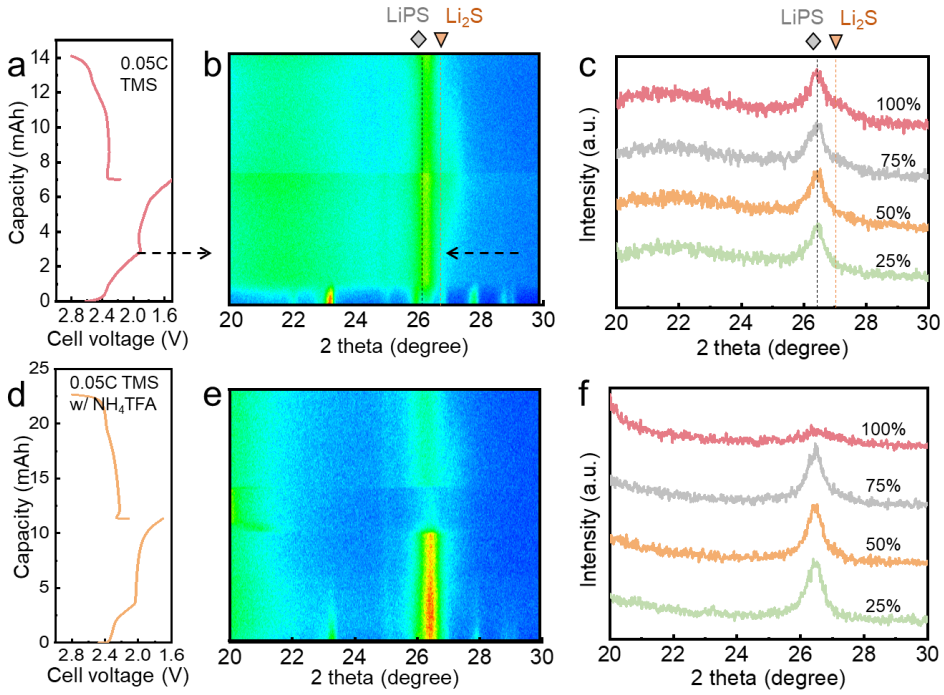

Figure 4. *Operando* XRD measurement of Li-S batteries based on the dual-phase electrolyte with and without NH_4TFA. From left to right: voltage profiles, XRD patterns, and selected XRD patterns at different depths of discharge. (a-c) 1.0 M LiTFSI in TMS cathode electrolyte. (d-f) 1.0 M LiTFSI and 0.2 M NH_4TFA in TMS cathode electrolyte. The cell was cycled at 0.05C rate.

Although the coulombic efficiency achieved by the GPE does not represent the highest among all liquid-based electrolyte systems, the coulombic efficiency can be further improved by modifying the current collector, electrolyte additives, etc.[34–37] The value of coulombic efficiencies became highly scattering when there was addition of 0.2 M NH_4TFA in TMS-based electrolytes, suggesting the anode corrosion induced by NH_4TFA is a non-negligible issue.

The long-term stability of anode and cathode were further studied in coin and pouch cells under low-Li-excess conditions (100 µm-thick Li foil as the anode, N/P = 3) (**Figure 5**). At a sulfur loading of 4.0 mg cm^{-2} and an E/S ratio of 7.5 µL mg^{-1} (electrolyte volume based on the cathode electrolyte), the coin full cell was assembled to understand the cyclability. With the GPE/TMS dual-

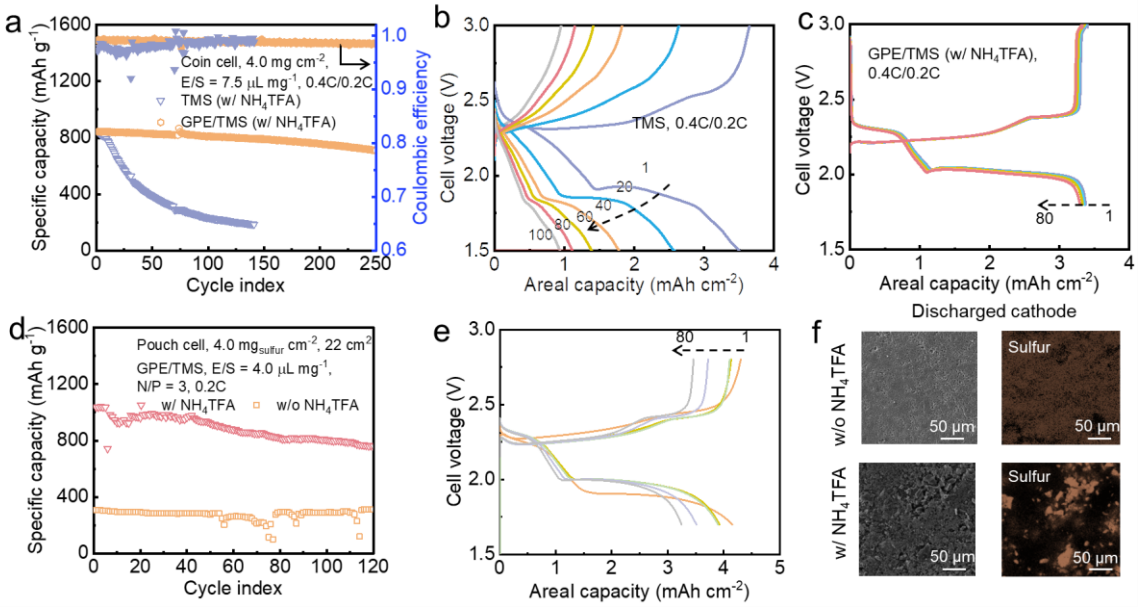

Figure 5. Full cell performance: (a-c) Cyclability of coin cells based on the dual-phase and single-phase electrolyte (formation cycles excluded). (b) Voltage profiles of coin cell with TMS-based single-phase electrolyte. (c) Voltage profiles of coin cell with dual-phase electrolyte. (d) Cyclability of pouch full cells based on the dual-phase electrolyte with and without NH_4TFA (formation cycles excluded). (e) Voltage profiles of pouch cells based on the dual-phase electrolyte (with NH_4TFA). The voltage profiles in Figure 5c, e are obtained at cycle 1, 20, 40, 60 and 80. (f) Morphology of the discharge products from the dual-phase electrolyte cells with and without NH_4TFA.

phase electrolyte, after 250 cycles, the coin cell achieved a specific capacity of 715 mAh g^{-1} (2.86 mAh cm^{-2}) and a high retention of 84.3% (0.4C discharge/0.2C charge). The coulombic efficiency of the full cell was constantly maintained above 98.5%. Rate performance of the coin cells based on dual-phase electrolyte was further evaluated (Figure S6); the cell retained an areal capacity of 2.43 mAh cm^{-2} (601 mAh g^{-1}) at 1C rate, which is around 65% of its capacity at 0.4C rate.

For the cell with single-phase electrolyte (1.0 M LiTFSI, 0.2 M NH_4TFA in TMS), the cell decayed to 35% of its initial capacity after 100 cycles. The cycled Li (at the charge state, after 250 cycles) displays a highly dense and uniform morphology for cell with GPE (Figure S5, Supporting Information).

Without DBE in the GPE, the dual-phase electrolyte coin cell (poly(DOL)-based GPE/|TMS) decayed to 64% of its initial capacity after 80 cycles (Figure S7, Supporting Information). The result clearly confirms that the GPE layer does not prevent lithium polysulfide crossover without the effect of phase separation.[38] Another benchmark, the single-phase electrolyte cell with the classical DOL/DME-based electrolyte, also decayed rapidly, retaining only 32% of its initial capacity after 80 cycles (Figure S7, Supporting Information). Furthermore, the cycling performance of a control cell with the configuration of Li | TMS | GPE(DBE) | TMS | sulfur cathode was measured (Figure S8); the cell could maintain stable cycling for 30 cycles, and experienced a fast capacity drop afterwards. This is consistent with our half-cell results that the Li metal displays a poor compatibility with the sulfolane-based electrolytes.

The lean-electrolyte Li-S pouch full cell enables a critical assessment of the sulfur cathode kinetics under practical conditions.[39] The cathode electrolyte to sulfur ratio was further reduced to be 4.0 μL mg^{-1} (Figure 5d, e). The overall weight ratio of GPE+TMS-LiTFSI versus sulfur is 7.7. Under such a low E/S ratio, the NH_4TFA additive performs a critical role in enhancing the

cathode kinetics. With the protection of GPE, after 120 cycles, the cell achieved a specific capacity of 770 mAh g^{-1} (3.08 mAh cm^{-2}), retaining 73% of its initial capacity. At 0.2C rate, with NH_4TFA additive, the cell displays an initial capacity 2.3 times higher than the cell without additive. Moreover, after discharge, at the cathode side, microsized Li_2S particles are observed for the cell, confirming the effects of additive on promoting Li_2S growth (Figure 5f).

Noticeably, there were no additional anode and cathode modifications, and cyclability can be improved further. The cell energy density (including anode, cathode, separator and electrolyte) is 215 Wh kg^{-1}, which can be increased further by reducing the amount of cathode electrolyte (see details in Table S1). This strategy provides an affordable solution to synergistically enhance cycle life and sulfur utilization. To scale up this design in multilayered pouch cells, we can confine the TMS-based cathode electrolyte in a polymer matrix and use bi-polar stacking methods to assemble the cells.[19]

3. Conclusion

In summary, we demonstrated a liquid-based dual-phase electrolyte design for lithium-sulfur batteries, which is highly compatible with the lean electrolyte cycling condition. The dual-phase electrolyte was designed by considering the mutual immiscibility of the two liquid phases and the mediator-solvating property. The selected dual-phase electrolyte system, polyDOL/DBE-LiTFSI || TMS-LiTFSI, enabled the confinement of corrosive electrolyte additive (NH_4TFA) and dissolved lithium polysulfide in the cathode region. The controlled diffusion resulted in improved Li-metal stability. Moreover, the use of highly solvating catholyte promises a high sulfur utilization. Consequently, a lithium-sulfur pouch cell with the dual-phase electrolyte exhibited a much more sustainable cycling performance. Without any electrode modifications, the cells were capable of cycling under lean electrolyte (E/S = 4.0 µL mg^{-1}), low Li excess (N/P = 3) conditions. The concept

of liquid-based dual-phase electrolytes can spur renewed efforts to meet the electrolyte requirements for various types of Li-metal batteries with aggressive battery chemistry.

4. Experimental method

All chemicals were used as received. Lithium bis(trifluoromethanesulfonyl)imide (LiTFSI), lithium nitrate, lithium hexafluorophosphate, dibutyl ether (DBE), tetramethylene sulfone (TMS), 1, 2-dimethoxyethane (DME), 1, 3-dioxolane (DOL), ammonia trifluoroacetate (NH_4TFA), Ketjen black (KB), multiwalled carbon nanotube (MWCNT), conductive carbon (Super P), polyethylene oxide (MW = 40,000), polyvinylpyrrolidone (MW = 55,000), pentaerythritol tetraacrylate (PETEA) and azobisisobutyronitrile (AIBN) were received from Sigma-Aldrich.

Gel polymer electrolyte and anode preparation

The liquid precursor was prepared in a two-step process. First, 1.0 M LiTFSI in DBE (33.3 vol%) was mixed with 1.0 M LiTFSI in DOL (66.7 vol%). Further, $LiPF_6$ (2.0 wt%), $LiNO_3$ (2.0 wt%), PETEA (2.0 wt%), and AIBN (0.5 wt%) additive were added into the liquid precursor (93.5 wt%). To prepare the GPE-protected anode, two phosphate-coated Celgard 2500 separators were first placed on the surface of Li foil, and then the liquid precursor was added (5.0 μL cm^{-2}). The Li metal and separator were sealed in a coin cell or a pouch cell to complete the thermal curing process (60 °C for 4 h). Owing to the high boiling point of dibutyl ether, negligible swelling was observed for the pouch cell after heating. The as-derived GPE-protected Li anode was taken out and used for cell assembly.

Cathode preparation

The sulfur cathodes were prepared by mixing 0.7 g of sulfur/KB, 0.1 g of Super P, and 0.1 g of MWCNT with 8 wt% polyethylene oxide and 2 wt% polyvinylpyrrolidone in 10 mL DI water.

The resultant slurry was blade-casted onto a carbon-coated Al foil and dried to yield cathodes with a loading of 4 ± 0.5 mg cm^{-2}. The electrolyte (based on TMS) to sulfur ratio was controlled to be 7.5 µL mg^{-1} for coin cell and 4.0 µL mg^{-1} for pouch cell, respectively. To understand the kinetics of sulfur conversion, one layer of carbon paper (Avcarb P-50, 1.1 cm^2) with a low surface area was in use. 50 µL liquid electrolyte containing 0.4 M Li_2S_6 (3.8 mg sulfur) and 1.0 M LiTFSI in TMS was added onto the carbon paper. The conditions with and without 0.2 M NH_4TFA additives were compared. The anode was all protected by the GPE during the kinetic measurement.

Cell assembly and test

CR2032 coin cells were assembled inside an argon-filled glovebox with O_2/H_2O level below 0.1 ppm. All full or half cells used one layer of Celgard 2325 separator filled with liquid electrolyte or GPE without specially specified. The TMS-based or DOL/DME-based liquid electrolytes were further added onto the 4.0 mg cm^{-2}-loading sulfur cathode when assembling the cell. This is followed by the addition of a separator and a 100 µm-thick (20 mAh cm^{-2}) Li metal foil. To evaluate the coulombic efficiency of Li stripping/plating, Li || Ni half cells were assembled by sandwiching the 600 µm-thick Li foil, a separator, and Ni foil.

Single-layered soft-packaging pouch half and full cells (cathode size: 5.3 cm × 4.8 cm) were fabricated like the coin cells. The tabs were welded onto the aluminum and nickel foil backings, respectively. The pouch cells were injected with a controlled amount of liquid electrolyte (360 µL) before being sealed.

The pressure control setup was built in-house. The pressure sensor was received from SIMBATOUCH Co.Ltd. In all coin and pouch cell tests, the anode was put on top of the cathode for two purposes: (i) gravity can prevent the inter-diffusion of electrolytes and (ii) TMS-based catholyte does not corrode the unprotected edge of Li-metal anode

Characterization

^{1}H and ^{19}F-NMR spectroscopies were performed via a Bruker Avance III 400 MHz NMR spectrometer. 128 scans of 4 each sample were performed, and the chemical shifts (δ) were calibrated using the residual solvent peak as 10 vol% d6-acetone was used as the internal standard. ^{19}F NMR was used to determine the LiTFSI salt concentration in TMS; 0.1 M CF_3COOLi (LiTFA) was fully dissolved in the TMS electrolyte as the benchmark.

To understand the Li^+ mobility, each ^{7}Li NMR scan was performed with a Varian VNMRS 600 MHz spectrometer at 23 °C. Sixteen scans were run at each temperature, with a relaxation delay of 60 s, a pulse width of 14.5 s, and an acquisition time of 2 s. In the case of overlapping peaks, the spectra were deconvoluted to process the raw data and determine peak locations. Samples were prepared in an argon filled glovebox consisting of either 0.2 M NH_4TFA or 0.2 M NH_4TFA and 0.1 M Li_2S_6 in TMS. 10 vol% d6-acetone was used as the internal standard.

Morphological characterization of sulfur cathode and Li-metal anode was carried out with a field-emission scanning electron microscopy (Vega), employing a source with a beam voltage of 10 kV.

Operando XRD analysis was performed with an Ultima IV X-ray diffractometer. The slurry containing sulfur/ketjen black and PEO/PVP binder in a weight ratio of 4 : 1 was coated onto a beryllium disk to reach an areal sulfur loading close to 8.0 mg cm^{-2}. A GPE-protected Li foil was in use. 32 µL cm^{-2} liquid electrolyte containing 0.2 M NH_4TFA additive was added to reach an E/S ratio of 4.0 µL mg^{-1}. The scan rate was 1 ° min^{-1}. And the operando XRD cell was cycled between 1.7 (or 1.5) and 3.0 V at a 0.05C rate with a Land CT2001A battery test system. Cyclic voltammetry and electrochemical impedance spectroscopy (EIS) (1 MHz ~ 0.1Hz, alternating current amplitude 50 mV) were performed on a potentiostat (Bio-logic, VMP3) via the two-electrode setup

Molecular dynamics (MD) simulations

The calculation was conducted with GROMACS 2020.4. DBE molecules display red color, while TMS molecules display yellow color (Figure 1e). First, a random amorphous model was constructed with packmol, containing 632 TMS molecules and 356 DBE molecules, and the initial model size was 6.37880 × 6.37880 × 6.37880 nm. The energy minimization process was performed on the initial model before the calculation. When the interatomic energy is less than 1000 kJ $mol^{-1}nm^{-1}$, the energy minimization process is complete. The energy-minimized system was pre-equilibrated with NPT for 1 ns, the temperature was controlled by the V-rescale method to 298.15K, and the Berendsen method was used to control the pressure for 1 atm. When the formal NPT molecular dynamics calculation was performed, the Nose-Hoover method was used to control the temperature at 298.15K, while the Parrinello-Rahman method controlled the pressure at 1atm, and the temperature-dependent time constant was set to 4 ps, and the pressure-dependent time constant to 10ps. All molecular dynamics calculations were performed with a step size of 2 fs, and the Lincs method was used to limit the bond lengths.

Supporting Information

Supporting Information is available from the Wiley Online Library or from the author. Molecular simulation results; EIS profiles; XRD profiles; SEM images.

Notes

The authors declare no competing financial interest.

Acknowledgment

This work was supported by the Assistant Secretary for Energy Efficiency and Renewable Energy, Office of Vehicle Technologies of the U.S. Department of Energy through the Advanced

Battery Materials Research (BMR) Program (Battery500 Consortium) award number DE-EE0007762.

Received: ((will be filled in by the editorial staff))
Revised: ((will be filled in by the editorial staff))
Published online: ((will be filled in by the editorial staff))

References

[1] A. Manthiram, Y. Fu, S.-H. Chung, C. Zu, Y.-S. Su, *Chem Rev* **2014**, *114*, 11751.

[2] G. Zhou, H. Chen, Y. Cui, *Nat Energy* **2022**, *7*, 312.

[3] M. Li, J. Lu, K. Amine, *ACS Nano* **2021**, *15*, 8087.

[4] R. Steudel, T. Chivers, *Chem Soc Rev* **2019**, *48*, 3279.

[5] Y. X. Ren, L. Zeng, H. R. Jiang, W. Q. Ruan, Q. Chen, T. S. Zhao, *Nat Commun* **2019**, *10*, 1.

[6] Y. X. Ren, T. S. Zhao, M. Liu, Y. K. Zeng, H. R. Jiang, *J Power Sources* **2017**, *361*, DOI 10.1016/j.jpowsour.2017.06.083.

[7] A. Bhargav, J. He, A. Gupta, A. Manthiram, *Joule* **2020**, *4*, 285.

[8] A. Manthiram, *Nat Commun* **2020**, *11*, 1.

[9] H. Y. Asl, A. Manthiram, *Nat Sustain* **2021**, *4*, 379.

[10] Q. Pang, A. Shyamsunder, B. Narayanan, C. Y. Kwok, L. A. Curtiss, L. F. Nazar, *Nat Energy* **2018**, *3*, 783.

[11] Y. X. Ren, H. R. Jiang, C. Xiong, C. Zhao, T. S. Zhao, *J Mater Chem A Mater* **2020**, *8*, 6902.

[12] A. Gupta, A. Bhargav, A. Manthiram, *ACS Energy Lett* **2020**, *6*, 224.

[13] H. Chu, H. Noh, Y.-J. Kim, S. Yuk, J.-H. Lee, J. Lee, H. Kwack, Y. Kim, D.-K. Yang, H.-T. Kim, *Nat Commun* **2019**, *10*, 188.

[14] S. Nanda, A. Bhargav, Z. Jiang, X. Zhao, Y. Liu, A. Manthiram, *Energy Environ Sci* **2021**.

[15] Y. Ren, K. B. Hatzell, *J Mater Chem A Mater* **2021**.

[16] Y.-X. Song, Y. Shi, J. Wan, S.-Y. Lang, X.-C. Hu, H.-J. Yan, B. Liu, Y.-G. Guo, R. Wen, L.-J. Wan, *Energy Environ Sci* **2019**, *12*, 2496.

[17] L. Cao, D. Li, T. Deng, Q. Li, C. Wang, *Angewandte Chemie* **2020**, *132*, 19454.

[18] J. Meng, Q. Tang, L. Zhou, C. Zhao, M. Chen, Y. Shen, J. Zhou, G. Feng, Y. Shen, Y. Huang, *Joule* **2020**, *4*, 953.

[19] S.-J. Cho, G. Y. Jung, S. H. Kim, M. Jang, D.-K. Yang, S. K. Kwak, S.-Y. Lee, *Energy Environ Sci* **2019**, *12*, 559.

[20] Y. Ko, H. Kim, S. Cho, K. M. Lee, G. Y. Jung, H. Park, S. H. Park, Y. J. Lee, Y. Bae, Y. Lee, *Adv Energy Mater* **2021**, *11*, 2102096.

[21] S.-J. Cho, G. Y. Jung, S. H. Kim, M. Jang, D.-K. Yang, S. K. Kwak, S.-Y. Lee, *Energy Environ Sci* **2019**, *12*, 559.

[22] M. Liu, D. Zhou, Y.-B. He, Y. Fu, X. Qin, C. Miao, H. Du, B. Li, Q.-H. Yang, Z. Lin, others, *Nano Energy* **2016**, *22*, 278.

[23] F.-Q. Liu, W.-P. Wang, Y.-X. Yin, S.-F. Zhang, J.-L. Shi, L. Wang, X.-D. Zhang, Y. Zheng, J.-J. Zhou, L. Li, *Sci Adv* **2018**, *4*, eaat5383.

[24] A. Gupta, A. Bhargav, J.-P. Jones, R. v Bugga, A. Manthiram, *Chemistry of Materials* **2020**, *32*, 2070.

[25] A. Gupta, A. Manthiram, *J Mater Chem A Mater* **2021**.

[26] A. Gupta, A. Bhargav, A. Manthiram, *Chemistry of Materials* **2021**, *33*, 3457.

[27] H. Pan, K. S. Han, M. H. Engelhard, R. Cao, J. Chen, J. Zhang, K. T. Mueller, Y. Shao, J. Liu, *Adv Funct Mater* **2018**, *28*, 1707234.

[28] H. Pan, K. S. Han, M. Vijayakumar, J. Xiao, R. Cao, J. Chen, J. Zhang, K. T. Mueller, Y. Shao, J. Liu, *ACS Appl Mater Interfaces* **2017**, *9*, 4290.

[29] G. Xu, J. Li, C. Wang, X. Du, D. Lu, B. Xie, X. Wang, C. Lu, H. Liu, S. Dong, *Angewandte Chemie* **2021**, *133*, 7849.

[30] J. Conder, R. Bouchet, S. Trabesinger, C. Marino, L. Gubler, C. Villevieille, *Nat Energy* **2017**, *2*, 1.

[31] Z. Li, Y. Zhou, Y. Wang, Y. Lu, *Adv Energy Mater* **2019**, *9*, 1802207.

[32] L. Lodovico, S. Milad Hosseini, A. Varzi, S. Passerini, *Energy Technology* **2019**, *7*, 1801013.

[33] X. Ren, S. Chen, H. Lee, D. Mei, M. H. Engelhard, S. D. Burton, W. Zhao, J. Zheng, Q. Li, M. S. Ding, *Chem* **2018**, *4*, 1877.

[34] X. Liu, A. Mariani, T. Diemant, M. E. di Pietro, X. Dong, M. Kuenzel, A. Mele, S. Passerini, *Adv Energy Mater* **2022**, 2200862.

[35] X. Liu, A. Mariani, M. Zarrabeitia, M. E. di Pietro, X. Dong, G. A. Elia, A. Mele, S. Passerini, *Energy Storage Mater* **2022**, *44*, 370.

[36] X. Liu, M. Zarrabeitia, A. Mariani, X. Gao, H. M. Schütz, S. Fang, T. Bizien, G. A. Elia, S. Passerini, *Small Methods* **2021**, *5*, 2100168.

[37] Y. Ren, A. Bhargav, W. Shin, H. Sul, A. Manthiram, *Angewandte Chemie* **2022**, *134*, e202207907.

[38] Q. Zhao, X. Liu, S. Stalin, K. Khan, L. A. Archer, *Nat Energy* **2019**, *4*, 365.

[39] J. Chen, J. Xiang, X. Chen, L. Yuan, Z. Li, Y. Huang, *Energy Storage Mater* **2020**, *30*, 179.

Table of Contents Entry

Two immiscible liquid-based electrolyte layers were applied for lithium-sulfur batteries. The sulfolane-based cathode electrolyte layer promotes lithium polysulfide dissolution and conversion kinetics. The anode electrolyte layer containing low polarity dibutyl ether repels sulfone and lithium polysulfide, preventing anode corrosion.

Key words: lithium-metal batteries, liquid electrolyte, pouch cell, phase separation

*Yuxun Ren, Arumugam Manthiram**

A dual-phase electrolyte for high-energy lithium-sulfur batteries

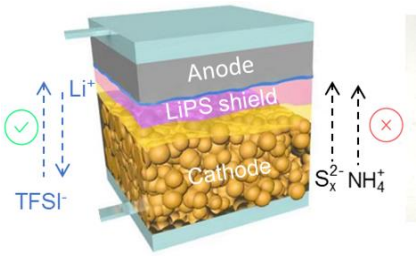

TOC

Supporting Information

A dual-phase electrolyte for high-energy lithium-sulfur batteries

*Yuxun Ren, Arumugam Manthiram**

Materials Science & Engineering Program and Texas Materials Institute

The University of Texas at Austin, Austin, TX, 78721, USA

*Corresponding author: Tel: +1-512-471-1791; fax: +1-512-471-7681

E-mail: manth@austin.utexas.edu (A. Manthiram)

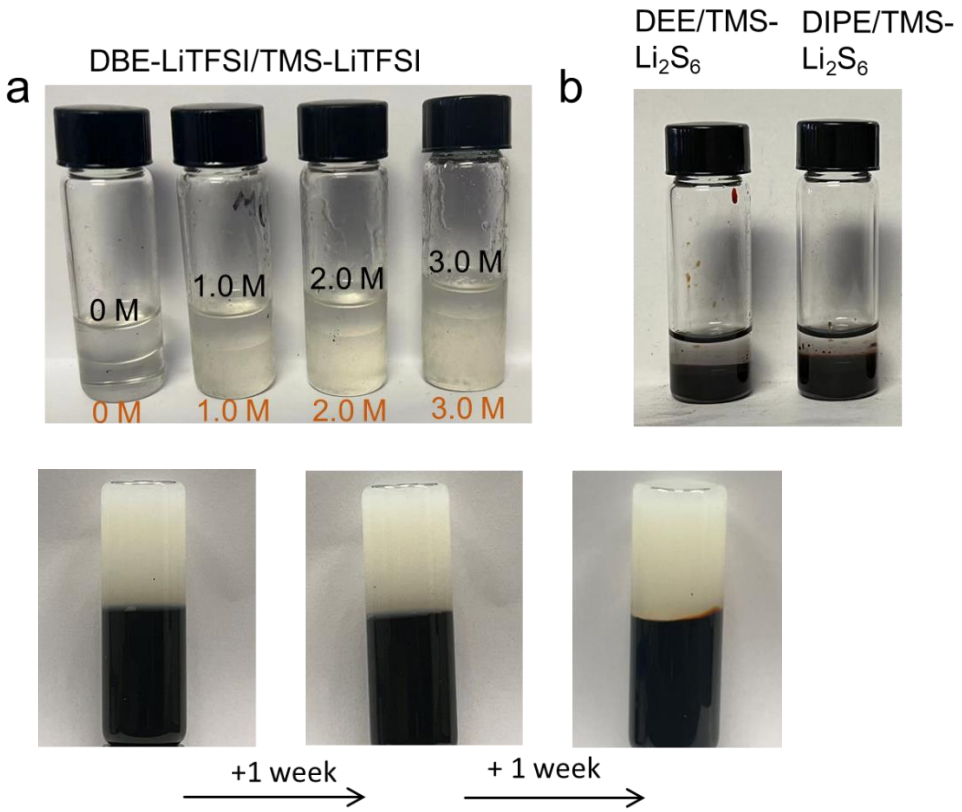

Figure S1. (a) Photos showing the phase separation of DBE-LiTFSI and TMS-LiTFSI electrolytes with different Li salt concentrations. (b) Phase separation between DEE and DIPE with 0.2 M Li_2S_6 in TMS. (c) Diffusion experiments showing the swelling behavior of GPE without DBE, and phase separation of GPE and TMS. 0.2 M Li_2S_6 was dissolved in TMS.

Supplementary note: as shown in Figure S1a, due to the difference in solvating power, when there is a moderate Li salt concentration (e.g. 1 or 2 M), the majority of the Li salt dissolved in DBE will migrate into the TMS phase. When the salt concentration increases further, the solvating power of the TMS phase decreases, and there will be more Li salt remaining in the DBE phase. Concentrated electrolyte is unwanted for sulfur redox reaction, therefore is not the focus of this study.

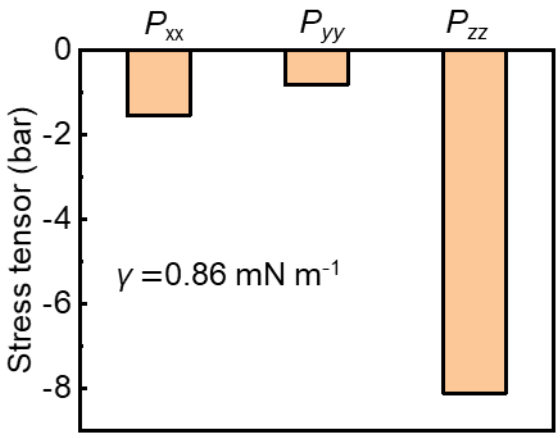

Figure S2. Pressure tensors along the x-, y-, and z-directions.

Supplementary note: P_{xx}, P_{yy}, and P_{zz} represent the pressure tensors along the x-, y-, and z-directions. Note that the z-axis is perpendicular to the interface. L_z denotes the box length in the z-direction. The average values of the interfacial tension (γ) obtained from MD simulations are derived from the following equation.[1]

$$\gamma = \frac{1}{2} L_z \left[P_{zz} - \frac{1}{2} (P_{xx} + P_{yy}) \right]$$

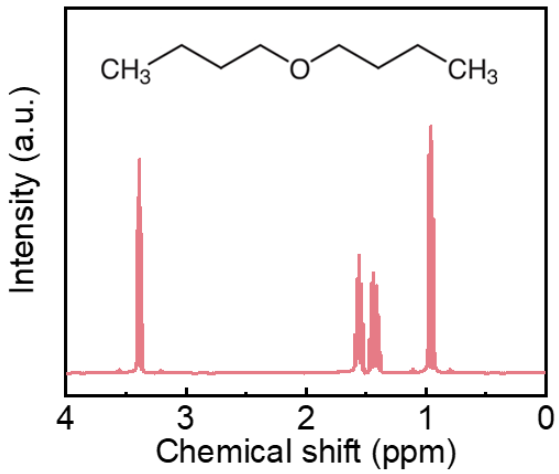

Figure S3. ^{1}H NMR spectra of DBE with NH_4TFA. There are only four peaks that can be assigned to DBE.

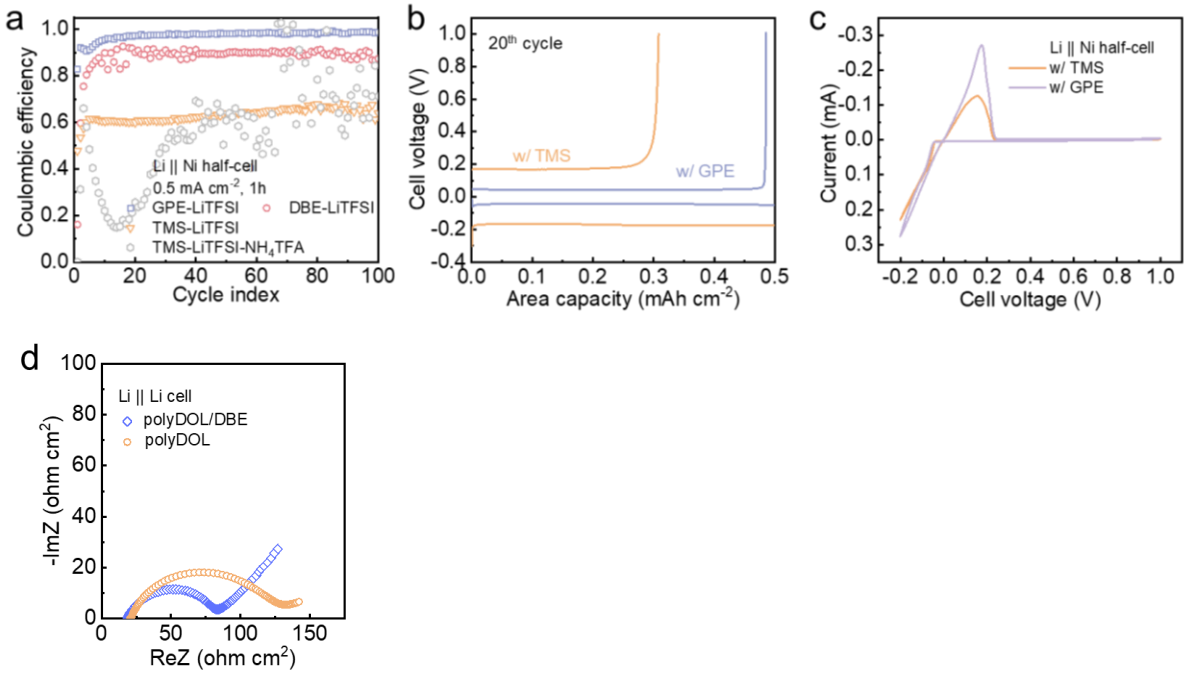

Figure S4. (a) Coulombic efficiency of Li || Ni half cells. (b) Corresponding voltage profiles of half cells with TMS-electrolyte or GPE. (c) Cyclic voltammetry profiles. (d) The interfacial resistance of symmetric Li || Li cells (after 5 formation cycles at 1.0 mA cm^{-2}, 1.0 mAh cm^{-2}) with different GPEs (polyDOL/DBE or polyDOL).

Supplementary note: as shown in Figure S4d, for the GPE without DBE, the symmetric Li || Li cell displays a higher interfacial resistance (52 ohm cm^2 versus 30 ohm cm^2). This indicates that DBE as a weakly solvating solvent is effective for enhancing the ion desolvation process and reducing the charge transfer resistance.

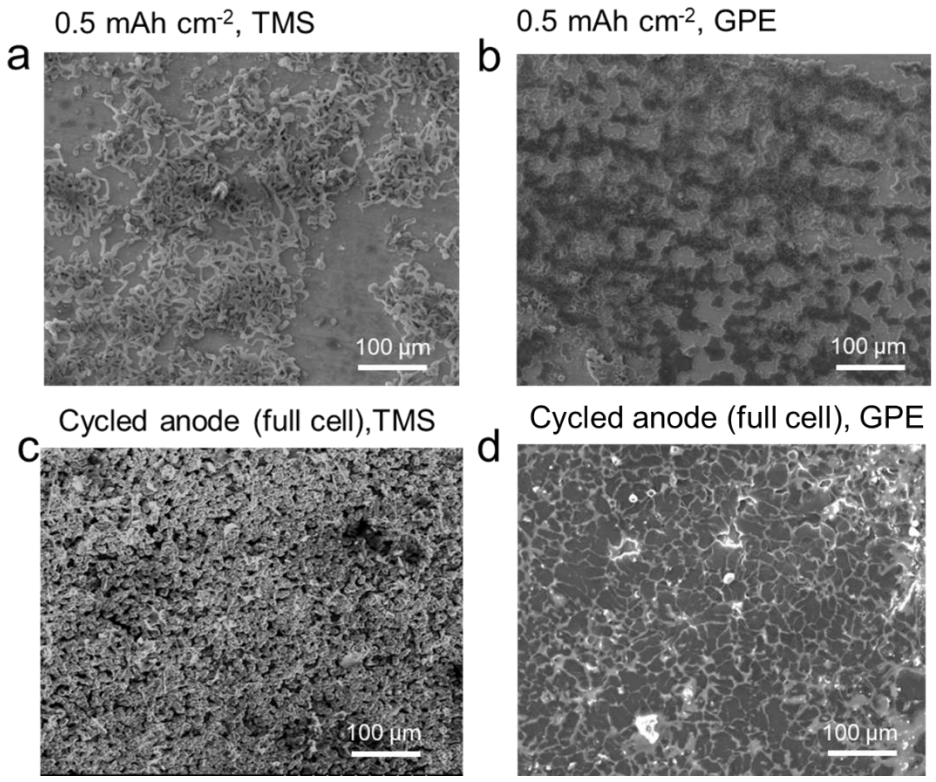

Figure S5. (a, b) Plated Li morphology (0.5 mAh cm^{-2}, 0,5 mA cm-2) from the discharged Li || Ni half cells with different electrolytes (TMS and GPE-based). (c, d) Cycled anode morphology with different electrolytes taken from Li-S coin cells (see cycling data in Figure 5a).

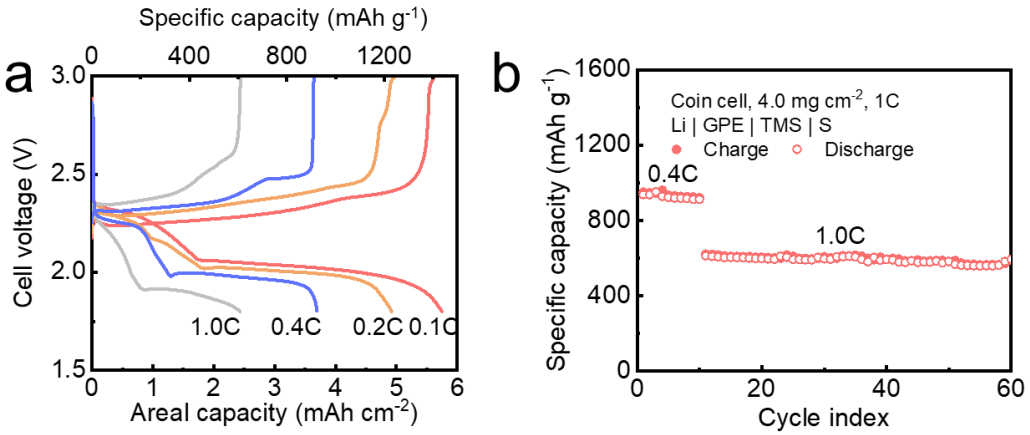

Figure S6. Rate performance of coin-type Li-S cell based on the dual-phase electrolyte. To avoid anode degradation, a smaller cathode (8 mm in diameter) and a large Li-metal anode (16 mm in diameter) were used.

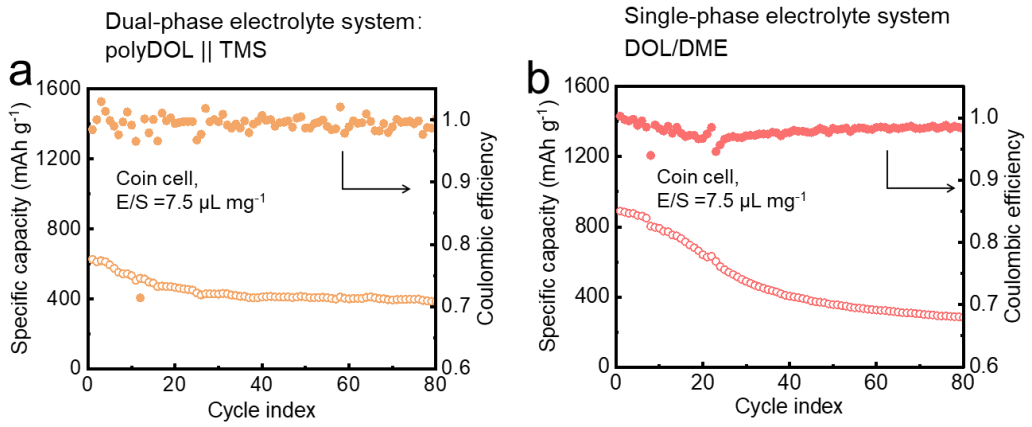

Figure S7. (a, b) Cyclability of Li-S coin cells based on the (a) dual-phase and (b) single-phase systems. For the cell with dual-phase electrolyte, the liquid precursor for anode GPE is 1.0 M LiTFSI, 0.2 M $LiNO_3$ in DOL. The cathode electrolyte is 1.0 M LiTFSI in TMS, consistent with the coin cell shown in Figure 5a. For the cell with single-phase electrolyte, the electrolyte is 1.0 M LiTFSI, 0.2 M $LiNO_3$ in DOL/DME; two fully wetted separators were used and then cathode electrolyte was added to reach the E/S ratio. Other cell parameters are identical to the cells described in Figure 5a.

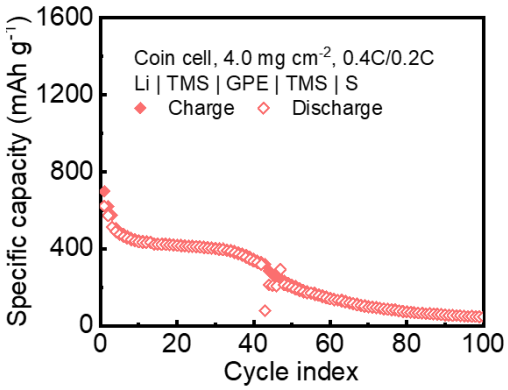

Figure S8. Cycling performance of a coin cell based on the configuration of Li | TMS | GPE(DBE) | TMS | sulfur.

Table S1. Parameters of dual-phase electrolyte Li-S full cells (4.0 mAh cm^{-2}) for energy density calculation

Cell components	Thickness (μm)	Weight (mg cm^{-2})
Li foil	100	5.34
GPE-filled separator	50	7.2
Sulfur cathode (40% porosity)	60	7.1
Liquid electrolyte at the cathode side	160	20.8
Total		**40.4**

Supplementary note: with an average cell voltage of 2.15 V, the gravimetry energy density of the cell is 212 Wh kg^{-1}. Noticeably, the cathode electrolyte was excessive to guarantee the cathode was fully wetted. The actual amount of liquid electrolyte required is 2.4 μL cm^{-2}, therefore, further increase of energy density is possible by rationally reducing the E/S ratio.